

**METHANE CONVERSION BY
SOLID ELECTROLYTE MEMBRANES**

FINAL REPORT

FOR THE PERIOD

JANUARY 1, 1989

TO

AUGUST 31, 1993

**Gas Research Institute
8600 West Bryn Mawr Avenue
Chicago, Illinois 60631**



METHANE CONVERSION BY SOLID ELECTROLYTE MEMBRANES

FINAL REPORT

for the period

(January 1, 1989 - August 31, 1993)

Prepared by

Michael Schwartz
James H. White
Ronald L. Cook
Anthony F. Sammells

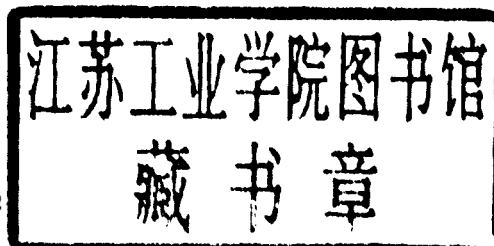
*Eltron Research, Inc.
2830 Wilderness Place
Boulder, CO 80301*

Eltron Project No. 30

for

GAS RESEARCH INSTITUTE
Contract No. 5089-260-182

GRI Project Manager
Kevin Krist
Sr. Project Manager,
Inorganic Chemistry
Physical Sciences Department



GRI DISCLAIMER

LEGAL NOTICE: This report was prepared by Eltron Research, Inc. as an account of work sponsored by the Gas Research Institute (GRI). Neither GRI, members of GRI, nor any person acting on behalf of either:

- a. Makes any warranty or representation, express or implied, with respect to the accuracy, completeness, or usefulness of the information contained in this report, or that the use of any apparatus, method, or process disclosed in this report may not infringe privately owned rights; or
- b. Assumes any liability with respect to the use of, or for damages resulting from the use of, any information, apparatus, method or process disclosed in this report.

RESEARCH SUMMARY

Title Methane Conversion by Solid Electrolyte Membranes

Contractor Eltron Research, Inc. GRI Contract Number: 5089-260-1824

Principal Investigators A. F. Sammells, M. Schwartz, R. L. Cook and J. H. White

Report Period January 1, 1989 - August 31, 1993
Report

Objective

- 1) 600°C solid-state fuel cells (SOFC) possessing new highly conductive solid electrolytes.
- 2) Effective, continuous oxidative coupling of methane at the lowest possible temperatures.

Technical Perspective and Approach

We are pursuing two approaches towards identifying intermediate temperature SOFC's. One approach involves identifying crystallographic parameters and ionic constituents for achieving rapid ionic mobility. This may lead to selecting solid electrolytes possessing high ionic conductivities which would provide small internal resistance losses in fuel cells. Initial focus has been on the influence of these parameters on activation energy, E_a , for ionic conduction. In future work we will additionally address the role of carrier density towards improving ionic conductivity in these materials. The second approach is involving the evaluation of metalloorganic chemical vapor deposition for depositing thin-film solid electrolytes to give SOFC's possessing intrinsically low internal resistance losses.

To provide electrocatalytic sites at the fuel cell anode compatible with either partial or complete methane oxidation, we are varying both electronic and ionic conductivity within solid-state lattice and lattice surface oxygen binding energies.

We are also exploring the use of mixed ionic and electronic conducting membranes for promoting methane oxidative dimerization at intermediate temperatures.

Results

We have:

- Shown how the activation energy, E_a , for anion conduction in perovskite electrolytes varies with thermodynamic and lattice geometric parameters. Perovskite lattices which favor low E_a for anion migration include: i) that the overall lattice possess a moderate metal-oxygen binding energy, and heats of formations ii) perovskite solid electrolytes possess large free volumes, iii) preferred $(r_{\text{critical}}/r_{\text{O}^{2-}})^2$ ratios for A-A-B saddle points $\cong 0.5$, and iv) that the lattice minimally polarizes the mobile anion by having

itself high polarizability.

- Identified perovskite-related structures possessing intrinsic anion vacancies that have high ionic conductivity.
- Incorporated new perovskite solid electrolytes into fuel cells which operate at intermediate temperatures.
- Tape-cast perovskite solid electrolytes in dense self-supporting films of 50 microns thickness.
- Designed and fabricated the hardware for a semi-internally manifolded intermediate temperature fuel cell stack.
- Identified criteria for selecting mixed ionic-electronic conducting perovskite membranes for methane oxidative dimerization.
- Found that more tightly bound O^- species present at the interfacial region give a higher probability towards promoting partial methane oxidation.
- Identified mixed-ionic-and electronic-conducting oxide candidates for SOFC electrodes and oxygen separation membranes.
- Prepared thin films of yttria stabilized zirconia (YSZ) using metalloorganic chemical vapor deposition.

Project Implications

This research sought to develop correlations underlying highly conductive solid electrolytes and employ more conductive electrolytes in laboratory fuel cells which operate at temperatures several hundreds of degrees below the 1000°C temperatures used in current solid oxide fuel cells (SOFCs). The goal of the research was to improve the reliability and cost of planar SOFCs through the use of electrolytes that could function under relatively mild temperatures. Although the research did not identify a candidate reduced-temperature SOFC device, its extensive findings provide a basis for further development. GRI does not plan to continue this contract.

TABLE OF CONTENTS

	<u>Page</u>
I. INTRODUCTION	1
II. PROJECT OBJECTIVE	1
A. Overall Project Objective	1
B. Project Description	2
C. Rationale for Undertaking Project	3
D. Projected Benefits to Natural Gas Consumers	3
III. RESULTS AND FINDINGS DURING THE REPORTING PERIOD	3
A. Rationale for Solid Electrolyte Selection	3
1. Some Preliminary Considerations	3
2. Influence of Dopant Concentration and Radii on E_a for Ionic Conduction	9
3. Influence of crystallographic and other factors on E_a .	13
4. Perovskites as solid electrolytes for intermediate temperature fuel cells	14
a. Perovskite structures	15
b. Perovskite thermodynamic stability	17
c. Minimizing electronic conductivity	18
d. Some ionic conductivity considerations in perovskite solid electrolytes	20
5. Parameters Found Influencing E_a in Perovskite Solid Electrolytes	22
a. Lattice free volumes	22
b. A-A-B perovskite crystallographic saddle point r_c	24
c. Thermodynamic considerations	26
d. Perovskite lattice polarizability	27
6. Results' Implications	32
B. EXPERIMENTAL EVALUATION OF PEROVSKITE SOLID ELECTROLYTES IN SOLID OXIDE FUEL CELLS	32
1. $\text{LaEr}_{0.9}\text{Ca}_{0.1}\text{O}_3$	32
2. $\text{LaEr}_{0.9}\text{Sr}_{0.1}\text{O}_{3-x}$	32

	<u>Page</u>
3. $\text{LaEr}_{0.9}\text{Ba}_{0.1}\text{O}_{3-x}$	35
4. $\text{LaSm}_{0.9}\text{Ca}_{0.1}\text{O}_{3-x}$	38
5. $\text{LaSr}_{0.1}\text{AlO}_{3-x}$	39
6. $\text{La}_{0.9}\text{Ba}_{0.1}\text{AlO}_{3-x}$	44
7. $\text{La}_{0.9}\text{Sr}_{0.1}\text{CaO}_3$	49
8. $\text{La}_{0.9}\text{Ba}_{0.1}\text{GaO}_{3-x}$	53
9. $\text{CaTi}_{0.7}\text{Ga}_{0.3}\text{O}_{3-x}$	53
10. $\text{CaTi}_{0.7}\text{In}_{0.3}\text{O}_{3-x}$	60
11. $\text{CaTi}_{0.8}\text{In}_{0.7}\text{O}_{3-x}$	63
12. $\text{CaTi}_{0.9}\text{In}_{0.1}\text{O}_{3-x}$	66
13. $\text{BaTb}_{1-y}\text{X}_y\text{O}_3$ (Y = In, Ca or Zn)	69
14. $\text{BaTh}_{0.9}\text{Gd}_{0.1}\text{O}_3$ (Performed Under a DOE-SBIR Program)	69
15. Result's Implications	75
C. HOMOGENEOUS SOFC STRUCTURES	80
D. THIN FILM SOFC STRUCTURES	93
E. MULTI-CELL DEVELOPMENT	96
1. Tape-Casting Perovskite Electrolytes	96
2. Design of Semi-Internally Manifolded Intermediate Temperature Fuel Cell	97
3. Results' Implications	98
F. CONCLUSIONS	98
G. PRESENTATIONS, PUBLICATIONS, AND PATENTS RELATED TO THIS WORK	98
1. Presentations	98
2. Publications	99
3. Patent	99

	<u>Page</u>
IV. REFERENCES	99
V. APPENDIX	103
A. SELECTION CRITERIA AND EVALUATION OF MIXED IONIC-ELECTRONIC CONDUCTING PEROVSKITE MEMBRANES FOR PARTIAL METHANE ACTIVATION	103
B. ELECTROCATALYSIS FOR PARTIAL METHANE OXIDATION	104
1. Partial Oxidation to C ₂ Species	104
2. Partial Methane Oxidation to CO.	108
3. Results' Implications	112

LIST OF FIGURES

<u>Figure No.</u>		<u>Page</u>
1	Correlation of $\ln(A)$ with E_a for doped ZrO_2 , CeO_2 and $BaCeO_3$.	5
2	Variation of ionic conductivity with dopant concentration for $(BaCeO_3)_{1-x}(Gd_2O_3)_x$ from calculations at Eltron using data in reference 14.	5
3	Variation in ionic conductivity for $(CeO_2)_{1-x}(Y_2O_3)_x$ electrolytes with dopant concentration from calculations at Eltron using data in reference 11.	6
4	Variation in ionic conductivity of $(ZrO_2)_{1-x}(M_2O_3)_x$ electrolytes with dopant concentration from calculation at Eltron using data in reference 16.	6
5	Plot of $\ln A$ vs. the enthalpy of migration for the solid electrolyte $BaCe_{1-x}Gd_xO_3$ ($x = 0.5, .10, .15, .20$).	8
6	Schematic temperature dependent conductivity plot illustrating conductivity ranges that can exist.	8
7	Plot of the activation energy for CeO_2 and $BaCeO_3$ based solid electrolytes as a function of dopant concentration.	10
8	Relationship of the activation energy for oxygen vacancy migration as a function of the ratio $r(\text{dopant})/r(\text{host})$ for doped ZrO_2 . ($10\%Ln_2O_3$).	11
9	Relationship of the activation energy for oxygen vacancy migration as a function of the ratio $r(\text{dopant})/r(\text{host})$ for doped $BaCeO_3$.	11
10	Plot of E_a for oxygen vacancy migration for 18% doped CeO_2 solid electrolytes as a function of ratio $r(\text{dopant})/r(\text{host})$.	12
11	Plot of the activation energy for oxygen vacancy migration for highly doped ZrO_2 solid electrolytes as a function of the ratio $r(\text{dopant})/r(\text{host})$.	12
12	Correlation of Radius ratio $r_{\text{dopant}}/r_{\text{host}}$ with E_a for $A^{2+}B^{4+}O_3$ and $A^{3+}B^{3+}O_3$ Perovskites.	13
13	A) Perovskite crystal structure showing relationship of BO_6 octahedra and A site cations, and B) Crystal structure showing distinct oxygen sites and buckling of BO_6 octahedra in orthorhombic perovskites.	16

<u>Figure No.</u>		<u>Page</u>
14	Representation of the brownmillerite $A_2B_2O_5$ perovskite phase showing alternating BO_6 octahedra (O) and BO_4 tetrahedra (T). \square = oxygen vacancies; \bullet = oxygen; \circ = B site cation. (A site cations not shown for clarity.)	16
15	Correlation of ΔH_f for ABO_3 perovskite oxides (from $AO + BO_2 \rightarrow ABO_3$) with the Goldschmidt Tolerance Factor. From Reference 47.	18
16	Plot of one-half the heat of formation of ABO_3 perovskites from the oxides AO and BO_2 against their band gap.	20
17	Schematic of defect site induced parasitic electronic conductivity in perovskite lattice.	20
18	Correlation between E_m and FV for undoped fluorite and perovskite solid electrolytes.	22
19	Correlation of FV with E_a for doped perovskites; diamonds are $A^{2+}B^{4+}O_3$ perovskites and circles $A^{3+}B^{3+}O_3$.	23
20	Geometry and calculation used for determining r_e (O^{2-} not to scale).	24
21	Correlation of r_e with E_{act} for undoped fluorite and perovskite solid electrolytes.	25
22	Plot E_a as a function of calculated r_e values for perovskite solid electrolytes.	25
23	Plot of E_a vs ABE for perovskite solid electrolytes.	26
24	Correlation of ΔH_f with E_a for perovskite solid electrolytes.	27
25	Coulombic contribution to interatomic potential experienced by a mobile point charge with $q = -2$ corresponding to O^{2-} species in a cubic perovskite lattice.	28
26	Coulomb potential modified by inclusion of overlap repulsion and short range attraction upon interaction of O^{2-} with the cubic perovskite lattice.	28
27	Coulombic potential modified by inclusion of overlap repulsion and short range attraction upon interaction of two O^{2-} in 220 plane with cubic perovskite lattice.	29
28	E_a vs MEP for undoped oxide electrolytes.	31

<u>Figure No.</u>		<u>Page</u>
29	Correlation of lattice ionic polarizability with activation energies for O^{2-} migration in perovskites.	31
30	Plot of ionic (σ_i) and electronic (σ_e) conductivity for the cell $H_2(3\% H_2O)/Ni/LaEr_{0.9}Ca_{0.1}O_3/LSM/O_2$.	33
31	Arrhenius plot of ionic conductivity for the cell $H_2(3\% H_2O)/Ni/LaEr_{0.9}Ca_{0.1}O_3/LSM/O_2$.	33
32	X-ray diffraction pattern of $LaEr_{0.9}Sr_{0.1}O_{3-x}$ after firing at $1500^\circ C$ for 12 hours.	34
33	X-ray diffraction pattern of $LaEr_{0.9}Sr_{0.1}O_{3-x}$ after firing at $1550^\circ C$ for 12 hours.	34
34	X-ray diffraction pattern of $LaEr_{0.9}Ba_{0.1}O_{3-x}$ sintered at $1400^\circ C$ for 12 hours.	35
35	X-ray diffraction pattern of $LaEr_{0.9}Ba_{0.1}O_{3-x}$ after firing at $1500^\circ C$ for 12 hours.	36
36	X-ray diffraction pattern of $LaEr_{0.9}Ba_{0.1}O_{3-x}$ after sintering at $1550^\circ C$ for 12 hours.	36
37	X-ray diffraction pattern of a sintered disk of $LaEr_{0.9}Ba_{0.1}O_{3-x}$ after sintering at $1600^\circ C$ for 4 hours.	37
38	Current-voltage plot for the cell: $H_2(3\%H_2O), Ni/LaEr_{0.9}Ba_{0.1}O_{3-x}/Ag, O_2(3\%H_2O)$ in the temperature range $550-700^\circ C$. $E_a = 0.94 eV$.	37
39	Arrhenius plot for the cell: $H_2(3\%H_2O), Ni/LaEr_{0.9}Ba_{0.1}O_{3-x}/Ag, O_2(3\%H_2O)$ in the temperature range $550-700^\circ C$. $E_a = 0.94 eV$.	38
40	Plot of ionic conductivity vs. $1000/T$ for $LaSm_{0.9}Ca_{0.1}O_3$ in the cell configuration $H_2(3\%H_2O)/Ni/LaSm_{0.9}Ca_{0.1}O_3/LSM/O_2$.	40
41	Arrhenius plot of $\ln(\sigma_i T)$ vs. $1000/T$ for $LaSm_{0.9}Ca_{0.1}O_3$ in the cell configuration $H_2(3\%H_2O)/Ni/LaSm_{0.9}Ca_{0.1}O_3/LSM/O_2$.	40
42	X-ray diffraction pattern of $La_{0.9}Sr_{0.1}AlO_{3-x}$ after sintering at $1200^\circ C$ for 12 hours.	41
43	X-ray diffraction pattern of $La_{0.9}Sr_{0.1}AlO_{3-x}$ after sintering at $1300^\circ C$ for 12 hours.	41
44	X-ray diffraction pattern of $La_{0.9}Sr_{0.1}AlO_{3-x}$ after sintering at $1400^\circ C$ for 12 hours.	42

<u>Figure No.</u>		<u>Page</u>
45	X-ray diffraction pattern of $\text{La}_{0.9}\text{Sr}_{0.1}\text{AlO}_{3-x}$ after sintering at 1500°C for 12 hours.	42
46	X-ray diffraction pattern of $\text{La}_{0.9}\text{Sr}_{0.1}\text{AlO}_3$ disk sintered at 1550°C for 4 hours.	43
47	Current-voltage plots for the cell: $\text{H}_2(3\% \text{H}_2\text{O}), \text{Ni}/\text{La}_{0.9}\text{Sr}_{0.1}\text{AlO}_{3-x}/\text{Ag}, \text{O}_2(3\% \text{H}_2\text{O})$ in the temperature range 550 - 700°C.	43
48	Arrhenius plot for the cell: $\text{H}_2(3\% \text{H}_2\text{O}), \text{Ni}/\text{La}_{0.9}\text{Sr}_{0.1}\text{AlO}_{3-x}/\text{Ag}, \text{O}_2(3\% \text{H}_2\text{O})$ in the temperature range 550-700°C. $E_a = 0.64 \text{ eV}$.	44
49	X-ray diffraction pattern of $\text{La}_{0.9}\text{Ba}_{0.1}\text{AlO}_{3-x}$ after sintering at 1200°C for 12 hours.	45
50	X-ray diffraction of $\text{La}_{0.9}\text{Ba}_{0.1}\text{AlO}_{3-x}$ after sintering at 1300°C for 12 hours.	45
51	X-ray diffraction pattern of $\text{La}_{0.9}\text{Ba}_{0.1}\text{AlO}_{3-x}$ after sintering at 1400°C for 12 hours.	46
52	X-ray diffraction pattern of $\text{La}_{0.9}\text{Ba}_{0.1}\text{AlO}_{3-x}$ after sintering 1500°C for 12 hours.	46
53	X-ray diffraction pattern of $\text{La}_{0.9}\text{Ba}_{0.1}\text{AlO}_{3-x}$ after a second sintering at 1500°C for 12 hours.	47
54	X-ray diffraction pattern of $\text{La}_{0.9}\text{Ba}_{0.1}\text{AlO}_{3-x}$ disk sintered at 1550°C for 12 hours.	47
55	Current-voltage plots for the cell: $\text{H}_2(3\% \text{H}_2\text{O}), \text{Ni}/\text{La}_{0.9}\text{Ba}_{0.1}\text{AlO}_{3-x}/\text{Ag}, \text{O}_2(3\% \text{H}_2\text{O})$ in the temperature range 600-700°C.	48
56	Arrhenius plot for the cell: $\text{H}_2(3\% \text{H}_2\text{O}), \text{Ni}/\text{La}_{0.9}\text{Ba}_{0.1}\text{AlO}_{3-x}/\text{Ag}, \text{O}_2(3\% \text{H}_2\text{O})$ in the temperature range 600-700°C. $E_a = 0.74 \text{ eV}$.	48
57	X-ray diffraction pattern of $\text{La}_{0.9}\text{Sr}_{0.1}\text{GaO}_{3-x}$ after sintering at 1200°C for 12 hours.	50
58	X-ray diffraction pattern of $\text{La}_{0.9}\text{Sr}_{0.1}\text{GaO}_{3-x}$ after sintering at 1300°C for 12 hours.	50
59	X-ray diffraction pattern of $\text{La}_{0.9}\text{Sr}_{0.1}\text{GaO}_{3-x}$ after sintering at 1500°C for 12 hours.	51

<u>Figure No.</u>		<u>Page</u>
60	X-ray diffraction pattern of $\text{La}_{0.9}\text{Sr}_{0.1}\text{GaO}_{3-x}$ disks prepared by sintering at 1500°C for 4 hours.	51
61	Current-voltage plot for the cell: $\text{H}_2(3\% \text{H}_2\text{O}), \text{Ni}/\text{La}_{0.9}\text{Sr}_{0.1}\text{GaO}_{3-x}/\text{Ag}, \text{O}_2(3\% \text{H}_2\text{O})$ in the temperature range 550-700°C.	52
62	Arrhenius plot for the cell: $\text{H}_2(3\% \text{H}_2\text{O}), \text{Ni}/\text{La}_{0.9}\text{Sr}_{0.1}\text{GaO}_{3-x}/\text{Ag}, \text{O}_2(3\% \text{H}_2\text{O})$ in the temperature range °C, $E_a = 0.96\text{eV}$.	52
63	X-ray diffraction pattern of $\text{La}_{0.9}\text{Ba}_{0.1}\text{GaO}_{3-x}$ after sintering at 1200°C for 12 hours.	54
64	X-ray diffraction pattern of $\text{La}_{0.9}\text{Ba}_{0.1}\text{GaO}_{3-x}$ after sintering at 1300°C for 12 hours.	55
65	X-ray diffraction pattern of $\text{La}_{0.9}\text{Ba}_{0.1}\text{GaO}_{3-x}$ after sintering at 1400°C for 12 hours.	55
66	X-ray diffraction pattern of $\text{La}_{0.9}\text{Ba}_{0.1}\text{GaO}_{3-x}$ after sintering at 1500°C for 12 hours.	56
67	X-ray diffraction pattern of a sintered disk of $\text{La}_{0.9}\text{Ba}_{0.1}\text{GaO}_{3-x}$ prepared by firing at 1500°C for 4 hours.	56
68	Current-voltage plots for the cell: $\text{H}_2(3\%\text{H}_2\text{O}), \text{Ni}/\text{La}_{0.9}\text{GaO}_{3-x}/\text{Ag}, \text{O}_2(3\%\text{H}_2\text{O})$ in the temperature range 550-700°C.	57
69	Arrhenius plot for the cell: $\text{H}_2(3\% \text{H}_2\text{O}), \text{Ni}/\text{La}_{0.9}\text{Ba}_{0.1}\text{GaO}_{3-x}/\text{Ag}, \text{O}_2(3\% \text{H}_2\text{O})$ in the temperature range 550-700°C, $E_a = 0.99\text{eV}$.	57
70	X-ray diffraction pattern of $\text{CaTi}_{0.7}\text{Ga}_{0.3}\text{O}_{3-x}$ powder fired at 1550°C for 4 hours.	58
71	X-ray diffraction pattern of a $\text{CaTi}_{0.7}\text{Ga}_{0.3}\text{O}_{3-x}$ disk after sintering at 1450°C for 4 hours.	59
72	Current-voltage plots for the cell: $\text{H}_2(3\% \text{H}_2\text{O}), \text{Ni}/\text{CaTi}_{0.7}\text{Ga}_{0.3}\text{O}_{3-x}/\text{Ag}, \text{O}_2(3\% \text{H}_2\text{O})$ in the temperature range 550-700°C.	59
73	Arrhenius plot for the cell: $\text{H}_2(3\% \text{H}_2\text{O}), \text{Ni}/\text{CaTi}_{0.7}\text{Ga}_{0.3}\text{O}_{3-x}/\text{Ag}, \text{O}_2(3\% \text{H}_2\text{O})$ in the temperature range 550-600°C. $E_a = 0.94\text{eV}$.	60

Figure No.Page

74	X-ray diffraction pattern of $\text{CaTi}_{0.7}\text{In}_{0.3}\text{O}_{3-x}$ after sintering at 1400°C for 12 hours.	61
75	X-ray diffraction pattern of $\text{CaTi}_{0.7}\text{In}_{0.3}\text{O}_{3-x}$ after a second sintering at 1400°C for 12 hours.	61
76	X-ray diffraction pattern of a $\text{CaTi}_{0.7}\text{In}_{0.3}\text{O}_{3-x}$ pellet after sintering at 1450°C for 4 hours.	62
77	Current-voltage plots for the cell: $\text{H}_2(3\% \text{H}_2\text{O})/\text{Ni}/\text{CaTi}_{0.8}\text{In}_{0.2}\text{O}_{3-x}/\text{Ag}, \text{O}_2(3\% \text{H}_2\text{O})$ in the temperature range 550-700°C.	62
78	Arrhenius plot for the cell: $\text{H}_2(3\% \text{H}_2\text{O}), \text{Ni}/\text{CaTi}_{0.8}\text{In}_{0.2}\text{O}_{3-x}/\text{Ag}, \text{O}_2(3\% \text{H}_2\text{O})$ in the temperature range 550-700°C. $E_a = 0.48\text{eV}$.	63
79	X-ray diffraction pattern of $\text{CaTi}_{0.8}\text{In}_{0.2}\text{O}_{3-x}$ powder fired at 1400°C for 12 hours.	64
80	X-ray diffraction pattern of $\text{CaTi}_{0.9}\text{In}_{0.1}\text{O}_{3-x}$ disk sintered at 1450°C for 4 hours.	65
81	Current-voltage plots for the cell: $\text{H}_2(3\% \text{H}_2\text{O}), \text{Ni}/\text{CaTi}_{0.9}\text{In}_{0.1}\text{O}_{3-x}/\text{Ag}, \text{O}_2(3\% \text{H}_2\text{O})$ in the temperature range 700-550°C.	65
82	Arrhenius for the cell: $\text{H}_2(3\% \text{H}_2\text{O}), \text{Ni}/\text{CaTi}_{0.9}\text{In}_{0.1}\text{O}_{3-x}/\text{Ag}, \text{O}_2(3\% \text{H}_2\text{O})$ in the temperature range 700-550°C. $E_a = 0.75\text{eV}$.	66
83	X-ray diffraction pattern of $\text{CaTi}_{0.9}\text{In}_{0.1}\text{O}_{3-x}$ powder after firing at 1400°C for 12 hours.	67
84	X-ray diffraction pattern of $\text{CaTi}_{0.9}\text{In}_{0.1}\text{O}_{3-x}$ disk sintered at 1450°C for 4 hours.	67
85	Current-voltage plots for the cell: $\text{H}_2(3\% \text{H}_2\text{O}), \text{Ni}/\text{CaTi}_{0.9}\text{In}_{0.1}\text{O}_{3-x}/\text{Ag}, \text{O}_2(3\% \text{H}_2\text{O})$ in the temperature range 700-550°C.	68
86	Arrhenius plot for the cell: $\text{H}_2(3\% \text{H}_2\text{O}), \text{Ni}/\text{CaTi}_{0.9}\text{In}_{0.1}\text{O}_{3-x}/\text{Ag}, \text{O}_2(3\% \text{H}_2\text{O})$ in the temperature range 700-600°C.	68
87	XRD pattern for $\text{BaTh}_{0.9}\text{Gd}_{0.1}\text{O}_3$. The compound was indexed to the cubic perovskite structure with $a = 4.487 \text{ \AA}$ ($\lambda = 1.54 \text{ \AA}$).	70

<u>Figure No.</u>		<u>Page</u>
88	Current-voltage curve for the fuel cell: $\text{H}_2(3\% \text{H}_2\text{O})/\text{BaTh}_{0.9}\text{Gd}_{0.1}\text{O}_3/\text{La}_{0.9}\text{Sr}_{0.1}\text{CoO}_3, \text{O}_2$ at 550°C. $\sigma = 8.7 \times 10^{-1} \text{Scm}^{-1}$.	71
89	Activation energy plots for $\text{BaTh}_{0.9}\text{Gd}_{0.1}\text{O}_3$ in the fuel cell: $\text{H}_2(3\% \text{H}_2\text{O})\text{Pd}/\text{BaTh}_{0.9}\text{Gd}_{0.1}\text{O}_3/\text{La}_{0.9}\text{Sr}_{0.1}\text{CoO}_3, \text{O}_2$ after one day 0.4eV of operation.	72
90	Nernstian type behavior for the concentration cell: $\text{H}_2(\text{He}), \text{Pd}/\text{BaTh}_{0.9}\text{Gd}_{0.1}\text{O}_3/\text{Pd}, \text{H}_2(\text{He})$ at 600°C, supporting predominant proton transport.	73
91	Plot of activation energy vs. $r(\text{dopant})/r(\text{host})$ for a series of perovskite solid electrolytes.	75
92	Plot of activation energy vs. free volume for a series of perovskite solid electrolytes.	77
93	Plot of activation energy vs. $(r_{\text{crit}}/r_{\text{oxide ion}})^2$ for a series of perovskite solid electrolytes.	77
94	Plot of activation energy vs. average bond energy for a series of perovskite solid electrolytes.	78
95	Plot of activation energy vs. heat of formation as calculated from the Goldschmidt tolerance factor for a series of perovskite solid electrolytes.	78
96	Plot of activation energy vs. molecular electronic polarizability for a series of perovskite solid electrolytes.	79
97	Schematic of <u>in situ</u> formation of PIN structure at perovskite-solid electrolyte leading to a homogeneous SOFC structure as first suggested by others. ⁸⁹	81
98	Current-voltage curve for the "fuel cell": $\text{H}_2(3\% \text{H}_2\text{O})\text{Ni}/\text{BaCe}_{0.9}\text{Gd}_{0.1}\text{O}_{2.95}/\text{O}_2$ absent of a distinct cathode. It was assumed that <u>in situ</u> formation of a p-region at the oxidant side region facilitated electrocatalysis for the O_2 reduction reaction at 680°C.	82
99	Current-voltage for the "fuel cell": $\text{H}_2, \text{Ni}/\text{BaCe}_{0.9}\text{Gd}_{0.1}\text{O}_{2.95}/\text{O}_2$ absent of a distinct cathode. It was assumed that <u>in situ</u> in formation of a p-region at the oxidant side facilitated electrocatalysis for the O_2 reduction at 680°C.	82

100	Current-voltage curves as a function of temperature for the cell: $H_2(3\% H_2O)/Ni/BaCe_{0.9}Gd_{0.1}O_{2.95}/Ag(3\% H_2O), O_2$.	84
101	Current-voltage curves at 680°C for the cell: $H_2, (3\% H_2O), Ni/BaCe_{0.9}Gd_{0.1}O_{2.95}/(3\% H_2O), O_2$.	84
102	Current-voltage curves at 800°C for the cell: $H_2, (3\% H_2O)/BaCe_{0.9}Gd_{0.1}O_{2.95}/Ag, (3\% H_2O), O_2$.	85
103	Current-voltage curves at 650°C for the cell: $H_2, (3\% H_2O)/BaCe_{0.9}Gd_{0.1}O_{2.95}/Ag(3\% H_2O), O_2$.	85
104	Electrochemical impedance spectrum at 700°C for the cell: $H_2O(3\% H_2O), Ni/BaCe_{0.9}Gd_{0.1}O_{2.95}/Ag(3\% H_2O), O_2$.	86
105	Electrochemical impedance spectrum at 680°C for the cell: $H_2, (3\% H_2O), Ni/BaCe_{0.9}Gd_{0.1}O_{2.95}/(3\% H_2O), O_2$.	87
106	Electrochemical impedance spectrum at 680°C for the cell: $H_2, (3\% H_2O)/BaCe_{0.9}Gd_{0.1}O_{2.95}/(3\% H_2O), O_2$.	87
107	Electrochemical impedance spectrum at 680°C for the cell: $H_2, (3\% H_2O), Ni/BaCe_{0.9}Gd_{0.1}O_{2.95}/Ni, (3\% H_2O), H_2$.	88
108	Electrochemical impedance spectrum at 680°C for the cell: $O_2, (3\% H_2O), Ag/BaCe_{0.9}Gd_{0.1}O_{2.95}/Ag, (3\% H_2O), O_2$.	88
109	Electrochemical impedance spectrum for the cell: $H_2, (3\% H_2O), Ni/BaCe_{0.9}Gd_{0.1}O_{2.95}/Ag, O_2(3\% H_2O)$ at 600°C.	89
110	Electrochemical impedance spectrum for the cell: $H_2(3\% H_2O), Ni/BaCe_{0.9}Gd_{0.1}O_{2.95}/Ag, O_2(3\% H_2O)$ at 800°C.	89
111	Electrochemical impedance spectrum for the cell: $H_2(H_2O), Ni/BaCe_{0.9}Gd_{0.1}O_{2.95}/Ag, O_2(H_2O)$ at 900°C.	90
112	Electrochemical impedance spectrum for the cell: $H_2(3\% H_2O)/BaCe_{0.9}Gd_{0.1}O_{2.95}/O_2(3\% H_2O)$ at 750°C.	90